Conjugate Heat Transfer in Stratified Two-Fluid Flows with a Growing Deposit Layer

H.Y. Li[1]*, Y.F. Yap[2], J. Lou[1], J.C. Chai[3], Z. Shang[4]
[1]Institute of High Performance Computing, A*STAR, Singapore
[2]Department of Mechanical Engineering, The Petroleum Institute, Abu Dhabi, UAE
[3]School of Computing and Engineering, University of Huddersfield, UK
[4]Center for Computation and Technology, Louisiana State University, LA 70803, USA

Abstract

The article presents a numerical model for moving boundary conjugate heat transfer in stratified two-fluid flows with a growing deposit layer. The model is applicable to other general moving boundary conjugate heat transfer problem in a two-fluid flow environment with deposition occurring simultaneously. The level-set method is adopted to capture the fluid-fluid interface and fluid-deposit front. The governing equations are solved using a finite volume method. Upon verification of the model, the effects of inlet velocity ratio, Damköhler number and thermal conductivity ratio on the flow, deposition as well as heat transfer are investigated. Generally, Nusselt number on the lower wall, Nu_{lx} and upper wall, Nu_{ux} show distinct features with the change of these parameters. Nu_{ux} increases with the increase of fluid 1 inlet velocity and the thermal conductivity of deposit layer, respectively. While it decreases with the increase of Damkholer number. Unlike the variation trend of Nu_{ux}, Nu_{lx} varies differently in the upstream and downstream along the channel, respectively under these parameters. A high fluid 1 velocity and a high thermal conductivity of deposit layer have a high Nu_{lx} upstream and a low Nu_{lx} downstream. However, a high Damkholer number results in a low Nu_{lx} upstream and a high Nu_{lx} downstream.

Keywords: conjugate heat transfer, stratified two-fluid flow, deposition, level-set method
* Corresponding author: Tel: +65-6419-1315; email: lih@ihpc.a-star.edu.sg

Nomenclature

C	particle concentration (kg/m^3)
c_p	specific heat (J/kg·K)
D	diffusion coefficient (m^2/s)
Da	Damkohler number
d	distance (m)
H	height of domain (m)
$H(\phi)$	smoothed heaviside function
k	thermal conductivity (W/m·K)
L	length of domain (m)
Nu	Nusselt number
$\hat{n}$	unit normal at the interface
Pe	Peclet number
Pr	Prandlt number
p	pressure (Pa)
$\vec{q}$	deposition flux (kg/ m^2·s)
Re	Reynolds number
r_d	reaction rate for deposition (m/s)
S	source term
$S(\phi)$	Sign function
T	temperature (^{o}C)
t	time (s)
$\vec{u}$	velocity vector (m/s)
x,y	Cartesian coordinate (m)

Greek Symbols

δ	height of the deposit region (m)
$\delta(\phi)$	Dirac delta function
Γ	interface
θ	dimensionless temperature
ϕ	level set function (m)
φ	component of $\vec{u}_{i,ext}$ (m/s)
ε	interface thickness (m)
μ	dynamic viscosity (kg/m·s)
ρ	density (kg/m^3)
Ω	domain of interest

Subscripts

b	bulk
d	deposit

d,ext	extension velocity
f	fluid
lx	local lower wall
ref	reference value
ux	local upper wall
w	wall
x	local
1	fluid 1 region
2	fluid 2 region
*	dimensionless

1. Introduction

A large number of engineering pipe flows involves two immiscible fluids with suspended particles. The prevailing two-fluid flow pattern depends on among others fluids' properties, flow configuration (horizontal, inclined or vertical) and relative flowrate [1]. For example, in a horizontal flow configuration, upon increasing the relative flowrate, the flow pattern progressive changes from bubbly, plug, stratified, wavy, slug to annular flow. Driven either physically or chemically, the suspended particles tend to deposit onto surfaces and form a solid deposit layer. The deposit layer is generally impermeable to flow and introduces extra flow resistance leading to a higher pressure drop. Often in these flows, heat transfer occurs. Heat transfer performance deteriorates because of additional thermal resistance of the deposit layer. Heat is now required to be conducted from the wall across the growing and increasingly thicker deposit layer before transferring to the flowing fluids. Engineering examples include wax deposition in oil-gas [2, 3] and oil-water [4, 5] flows, asphaltene deposition in oil-water [6] and oil-gas (CO_2) [7] flows, hydrate deposition in water-gas flow [8, 9], fouling in two-phase heat exchanger [10] and fouling in flow boiling [11, 12].

From a modeling point of view, this is a moving boundary conjugate heat transfer problem. There are two boundaries evolving both spatially and temporally, i.e. the fluid-fluid interface and the fluid-deposit front. At these boundaries, various transport processes involving mass, momentum and energy interact with each other in a fully-coupled manner. In particular, coupling of heat transfer in the fluids

to that in the deposit layer requires a conjugate approach. The modeling framework generally requires six components to capture (a) fluid-fluid interface, (b) fluid-deposit front; to model (c) fluid transport, (d) particle transport, (e) particle deposition and (f) energy transport. Good prediction of the interaction between transport processes requires accurate determination of the moving boundaries. The fluid-fluid interface can be handled using either a front-tracking approach [13] or a front-capturing approach, e.g. VOF [14] and level-set [15] methods. For fluid-deposit front, apart from VOF and level-set methods, it can also be treated using enthalpy–porosity [16] and total concentration [17] methods. To model particle deposition, i.e. the actual attachment of the particles onto the fluid-deposit front, a critical length coupled with a sticking probability [18, 19] or an m-th order deposition reaction [20, 21] can be employed. Fluid transport entails prediction of the fluids' velocity and pressure fields. For particle transport, the transient particle distribution is determined using either a Langrangian or Eulerian approach [22]. Energy transport accounts for determining the temperature field. It should be stressed here again that all these six components of the model are fully-coupled together. Modeling then becomes challenging.

Modeling work of such moving boundary conjugate heat transfer problem is scarcely limited in the existing literatures. These existing modeling works will be briefly discussed. To make the problem more tractable, simplifications were often made in the existing modeling works. Therefore, these models do not necessarily have all the six components and may not follow structurally the above framework.

Huang *et al.* [4] developed a model of wax deposition in a two-dimensional non-isothermal oil-water laminar stratified channel flow. The results presented highlight the importance of incorporating the movement of the oil-water interface for a more accurate deposition prediction, not accounted for in previous studies. For this flow configuration, there exists a priori good geometrical understanding of both the oil-water interface and oil-wax front. The deposition is assumed to be controlled by the particle diffusion into the deposit layer. The flow is modeled as quasi-steady and unidirectional, and thus allowing a simple analytical expression of the velocity field be derived. The interface is then

determined such that mass conservation is satisfied. Particle and energy transports are governed only by axial convection and transverse diffusion. The approach suggested serves well for stratified flow but is generally challenging to be extended to other flow configurations with more general interfacial geometries.

Ramirez-Jaramillo *et al.* [23] proposed a numerical model to simulate asphaltene deposition in a three-phase flow system. These three immiscible phases are oil, gas and water and form a rheological fluid. The flow is determined from flow-pattern specific semi-empirical correlations without tracking or capturing the fluid-fluid interface. Convection heat transfer is considered with empirical correlation used in determining the heat transfer coefficient. Dissolved asphaltene in oil is assumed driven radially by diffusion and precipitates on the wall surface. A thermodynamic model is then utilized to predict this asphaltene precipitation process. In the model, the asphaltene deposit layer formed on the wall is subjected to removal due to shear force. Therefore, the growth of the deposit layer is driven asphaltene precipitation but is retarded by shear removal.

Apte *et al.* [24] developed a model to investigate paraffin deposition in multiphase flowlines and wellbores. The flow is assumed steady and one-dimensional. For a one-dimensional flow, tracking of the fluid-fluid interface and fluid-deposit front are not required. This greatly simplifies the model. Fluid transport is determined using multiphase mechanistic models for both flow pattern identification and pressure gradient prediction. Regardless of flow pattern, heat transport is modeled by assuming a homogeneous mixture in a steady one-dimensional configuration. The reduction in heat transfer due to the deposit layer is conjugated. An additional thermodynamic model is also incorporated to predict the formation of solid "wax" fraction, i.e. the to-be-deposited particles in the above mentioned framework. The thermodynamic model also provides fluid properties. For particle deposition, it is assumed that all the solid "wax" diffused to the pipe wall deposits. Both Brownian (concentration gradient) and thermophoretic (radial temperature gradient) diffusions are accounted for.

Nasria and Dabir [6] developed a network model for prediction of asphaltene deposition in porous media for two-phase flow. Deposition in porous media changes among others the permeability and porosity. In a network model, fluid transport is governed by capillary equilibrium between phases with fluid displacement of either the drainage or the imbibition type. The fluid-fluid interface is not captured. Asphaltene precipitation is quantified by a thermodynamic model with the asphaltene particles sizes estimated. In a porous media at the pore-throat scale level, asphaltene deposition occurs due to adsorption and mechanical trapping.

Given the limited work on conjugate heat transfer in two-fluid flow with particle deposition, the present work is undertaken to complement the existing literature. Specifically, the current work focuses on conjugate heat transfer in stratified two-fluid flow with a growing deposit layer. Of particular interest in the current model over the above mentioned modeling works is having both fluid-fluid interface and fluid-deposit front captured while simultaneously coupled in a fully manner to the fluid transport, particle transport, energy transport and particle deposition. Similar framework although without heat transfer has been implemented earlier for particle deposition in single-[25] and two-fluid [26] flow environment. Conjugate heat transfer in single-fluid flow environment has also been demonstrated [27]. The objective of the present work is to develop a conjugate heat transfer model in a stratified two-fluid system. The current framework is more generic in the sense that it can be applied to a wide range applications compared with that of conjugate heat transfer in single-fluid flow system [27]. With the model developed in this paper, the effects of inlet velocity ratio, Damköhler number and thermal conductivity ratio on the flow, deposition as well as heat transfer in terms of Nusselt number at lower wall and upper wall are investigated.

2. Problem Description

Figure 1 shows the schematic diagram of the two-dimensional channel. The domain consists of three regions, i.e. the fluid 1 region Ω_1, the fluid 2 region Ω_2 and the deposit region Ω_d. The fluid 1 and the fluid 2 regions are separated by the fluid-fluid interface Γ_f. The two fluids are immiscible with

each other. On the other hand, the fluid 1 and the deposit regions are separated by the fluid-deposit front Γ_d. The deposit region is impermeable to the fluids. Initially, the channel is clean without any deposit formed. At $t=0$, the two fluids, i.e. fluid 1 and fluid 2, flow into the channel both at a constant temperature of T_{in}. Fluid 1 carries suspended particles. These particles gradually deposit onto the lower wall of the channel forming a deposit layer of thickness δ, i.e. Ω_d. This deposit layer becomes thicker over time as more and more particles deposited. Both the upper and the lower walls are maintained at a temperature of T_w where $T_w > T_{in}$. Heat transfer mode at the upper wall and lower wall is different. For the upper wall, the incoming heat from the upper wall is directly absorbed by fluid 2 and then convected downstream. However, for the lower wall, the deposit layer presents an extra thermal resistance. This extra thermal resistance increases as the deposit layer grows. As a result, the incoming heat has to be conducted across the increasingly thicker solid deposit layer before transferred into fluid 1, i.e. a moving boundary conjugate heat transfer problem. Effectively, the flow of the two fluids, transport and deposition of the particles and conjugate transfer of heat are all coupled together. Modeling this is the focus of the current study.

3. Mathematical Formulation

3.1 Fluid-Fluid Interface

In this article, the level-set method is adopted to capture the fluid-fluid interface Γ_f [15]. It is represented by a level-set function as

$$\phi_f \equiv \begin{cases} -d_f, & \text{if } \vec{x} \in \Omega_2 \\ 0, & \text{if } \vec{x} \in \Gamma_f \\ +d_f, & \text{if } \vec{x} \in \Omega_1 \cup \Omega_d \end{cases} \tag{1}$$

where d_f is the shortest distance from the fluid-fluid interface. The motion of the fluid-fluid interface is governed by

$$\frac{\partial \phi_f}{\partial t} + \vec{u} \cdot \nabla \phi_f = 0 \tag{2}$$

where $\vec{u}$ is the fluid velocity. Numerically, ϕ_f will drift away from being a distance function gradually when Eq. (2) is solved. To alleviate this problem, redistancing is required [28]. In addition, the local mass correction [29] is performed to alleviate the mass loss or mass gain problem in the level-set method.

3.2 Fluid-Deposit Front

The fluid-deposit front Γ_d is represented by a level-set function defined as

$$\phi_d \equiv \begin{cases} -d_d, \text{if } \vec{x} \in \Omega_d \\ 0, \quad \text{if } \vec{x} \in \Gamma_d \\ +d_d, \text{if } \vec{x} \in \Omega_1 \cup \Omega_2 \end{cases} \tag{3}$$

where d_d is the shortest distance from the fluid-deposit front. The motion of the fluid-deposit front is governed by

$$\frac{\partial \phi_d}{\partial t} + \vec{u}_{d,ext} \bullet \nabla \phi_d = 0 \tag{4}$$

where $\vec{u}_{d,ext}$ is a velocity field extended from the velocity of the fluid-deposit front $\vec{u}_d$. The extension is constructed in such a way that $\vec{u}_{d,ext}$ is constant along the curve normal to the fluid-deposit front. This is achieved using the approach suggested in [30] as

$$\frac{\partial \varphi}{\partial t} + S(\phi)\hat{n} \bullet \nabla \varphi = 0 \tag{4a}$$

$$S(\phi) = \begin{cases} -1, & \text{if } \phi_d < 0 \\ 0, & \text{if } \phi_d = 0 \\ +1, & \text{if } \phi_d > 0 \end{cases} \tag{4b}$$

where φ is the component of $\vec{u}_d$.

The deposition process is modeled as a first order deposition reaction. The deposition flux is given by

$$\vec{q} = -\rho_d \vec{u}_d = -r_d C \hat{n}_d \tag{5}$$

where ρ_d, r_d, C and $\hat{n}_d$ are the density of the deposit, the deposition reaction rate, the particle concentration and unit normal vector pointing into the fluid 1 region respectively. Rearrangement of Eq. (5) gives the velocity of the depositing front as

$$\vec{u}_d = \frac{r_d C \hat{n}_d}{\rho_d} \tag{6}$$

where the unit vector $\hat{n}_d$ is evaluated as

$$\hat{n}_d = \frac{\nabla \phi_d}{|\nabla \phi_d|} \tag{7}$$

3.3 Conservation Equations

The conservation equations governing the transport of mass, momentum, particle and energy for the problem are given by

$$\nabla \bullet \vec{u} = 0 \tag{8}$$

$$\frac{\partial(\rho \vec{u})}{\partial t} + \nabla \bullet (\rho \vec{u} \vec{u}) = -\nabla p + \nabla \bullet \left[\mu(\nabla \vec{u} + \nabla \vec{u}^T)\right] \tag{9}$$

$$\frac{\partial C}{\partial t} + \nabla \bullet (\vec{u} C) = \nabla \bullet (D \nabla C) - r_d C \delta(\phi_d) |\nabla \phi_d| \tag{10}$$

$$\frac{\partial(\rho c_p T)}{\partial t} + \nabla \bullet (\rho c_p \vec{u} T) = \nabla \bullet (k \nabla T) \tag{11}$$

where $\vec{u}$, p, C and T are respectively fluid velocity, pressure, particle concentration and temperature. The required thermo-physical properties in the conservation equations are density ρ, viscosity μ, diffusion coefficient D, specific heat c_p and thermal conductivity k.

Both surface tension and gravity have small effect on the flow, in particular no effect in the fully-developed region [31]. These factors are not included into the momentum equation. If desired, surface tension can be incorporated using the Continuum Surface Force model. The second term on the right hand side of Eq. (10), i.e. $-r_d C\delta(\phi_d)|\nabla\phi_d|$, accounts for the amount of particles transformed into deposit at the fluid-deposit front. It is localized to be only non-zero around the fluid-deposit front using a smoothed Dirac function defined as

$$\delta(\phi) \equiv \begin{cases} \dfrac{1+\cos[\pi(\phi-\varepsilon)/\varepsilon]}{2\varepsilon}, & \text{if } 0 \le \phi \le 2\varepsilon \\ 0, & \text{otherwise} \end{cases} \tag{12}$$

During the movement of the fluid-deposit front, some of the particles near the front might be trapped inside the deposit region. Besides, during the movement of the fluid-fluid interface, some of the particles near the interface may drift into the fluid 2 region. If left untreated, the amount of trapped/drifted particles increases with time. To alleviate this problem, these trapped/drifted particles will be redistributed evenly to all other CVs of the fluid 1 region following the approach suggested in [17].

By introducing a smoothed Heaviside function given by

$$H(\phi) = \begin{cases} 0, & \text{if } \phi < -\varepsilon \\ \dfrac{\phi+\varepsilon}{2\varepsilon} + \dfrac{1}{2\pi}\sin\left(\dfrac{\pi\phi}{\varepsilon}\right), & \text{if } |\phi| \le \varepsilon \\ 1, & \text{if } \phi > +\varepsilon \end{cases} \tag{13}$$

The thermo-physical properties in the conservation equations can be evaluated as

$$\rho = \begin{cases} \rho_1, & \text{if } \phi_f > \varepsilon, \ \ \phi_d > \varepsilon \\ (\rho_1 - \rho_2)H(\phi_f) + \rho_2, & \text{if } |\phi_f| \le \varepsilon, \ \ \phi_d > \varepsilon \\ \rho_2, & \text{if } \phi_f < -\varepsilon, \ \ \phi_d > \varepsilon \\ (\rho_1 - \rho_d)H(\phi_d) + \rho_d, & \text{if } |\phi_d| \le \varepsilon, \ \ \phi_d \le \varepsilon \\ \rho_d, & \text{otherwise} \end{cases} \tag{14}$$

$$\mu = \begin{cases} \mu_1, & \text{if } \phi_f > \varepsilon,\ \ \phi_d > \varepsilon \\ \left[\dfrac{H(\phi_f)}{\mu_1} + \dfrac{1-H(\phi_f)}{\mu_2}\right]^{-1}, & \text{if } |\phi_f| \le \varepsilon,\ \ \phi_d > \varepsilon \\ \mu_2, & \text{if } \phi_f < -\varepsilon,\ \ \phi_d > \varepsilon \\ \left[\dfrac{H(\phi_d)}{\mu_1} + \dfrac{1-H(\phi_d)}{\mu_d}\right]^{-1}, & \text{if } |\phi_d| \le \varepsilon,\ \ \phi_d \le \varepsilon \\ \mu_d, & \text{otherwise} \end{cases} \tag{15}$$

$$c_p = \begin{cases} c_{p1}, & \text{if } \phi_f > \varepsilon,\ \ \phi_d > \varepsilon \\ (c_{p1} - c_{p2})H(\phi_f) + c_{p2}, & \text{if } |\phi_f| \le \varepsilon,\ \ \phi_d > \varepsilon \\ c_{p2}, & \text{if } \phi_f < -\varepsilon,\ \ \phi_d > \varepsilon \\ (c_{p1} - c_{pd})H(\phi_d) + c_{pd}, & \text{if } |\phi_d| \le \varepsilon,\ \ \phi_d \le \varepsilon \\ c_{pd}, & \text{otherwise} \end{cases} \tag{16}$$

$$k = \begin{cases} k_1, & \text{if } \phi_f > \varepsilon,\ \ \phi_d > \varepsilon \\ \left[\dfrac{H(\phi_f)}{k_1} + \dfrac{1-H(\phi_f)}{k_2}\right]^{-1}, & \text{if } |\phi_f| \le \varepsilon,\ \ \phi_d > \varepsilon \\ k_2, & \text{if } \phi_f < -\varepsilon,\ \ \phi_d > \varepsilon \\ \left[\dfrac{H(\phi_d)}{k_1} + \dfrac{1-H(\phi_d)}{k_d}\right]^{-1}, & \text{if } |\phi_d| \le \varepsilon,\ \ \phi_d \le \varepsilon \\ k_d, & \text{otherwise} \end{cases} \tag{17}$$

Note that, the solid deposit is modeled as a fluid with extremely large viscosity, i.e. by setting μ_d to a large number say 10^{30} in Eq. (15).

For ease of results discussion in Section 4, the following dimensionless quantities are defined:

$$x^* = x/H,\ y^* = y/H,\ t^* = tu_{ref}/H \tag{18a}$$

$$\vec{u}^* = \vec{u}/u_{ref},\ p^* = p/\rho_{ref}u_{ref}^2,\ C^* = C/\rho_d,\ \theta = \frac{T - T_{ref}}{T_w - T_{ref}} \tag{18b}$$

$$\rho^* = \rho/\rho_{ref},\ \mu^* = \mu/\mu_{ref},\ c_p^* = c_p/c_{pref},\ k^* = k/k_{ref} \tag{18c}$$

Properties of fluid 2 are selected as the reference (*ref*). u_{ref} and T_{ref} are set respectively to the fluid 2 inlet velocity and temperature. Substitution of Eqs. (20) into the conservation equations (Eqs. 8-11) gives

$$\nabla^* \bullet \vec{u}^* = 0 \tag{19}$$

$$\frac{\partial(\rho^* \vec{u}^*)}{\partial t^*} + \nabla^* \bullet (\rho^* \vec{u}^* \vec{u}^*) = -\nabla^* p^* + \frac{1}{\mathrm{Re}} \nabla^* \bullet \left[\mu^* (\nabla^* \vec{u}^* + \nabla^* \vec{u}^{*T}) \right] \tag{20}$$

$$\frac{\partial C*}{\partial t*} + \nabla* \bullet (\vec{u}* C*) = \nabla* \bullet (\frac{1}{Pe} \nabla* C*) - \frac{Da}{Pe} C* \delta*(\phi_d) |\nabla \phi_d| \tag{21}$$

$$\frac{\partial(\rho^* c_p^* \theta)}{\partial t^*} + \nabla^* \bullet (\rho^* c_p^* \vec{u}^* \theta) = \frac{1}{\mathrm{Re}} \frac{1}{\mathrm{Pr}} \nabla^* \bullet (k^* \nabla^* \theta) \tag{22}$$

where the Reynolds (Re), Prandlt (Pr), Peclet (Pe) and Damkohler (Da) numbers are given respectively by:

$$\mathrm{Re} = \frac{\rho_{ref} u_{ref} H}{\mu_{ref}} \tag{23a}$$

$$\mathrm{Pr} = \frac{c_{p_{ref}} \mu_{ref}}{k_{ref}} \tag{23b}$$

$$Pe = u_{ref} H / D \tag{23c}$$

$$Da = r_d H / D \tag{23d}$$

3.4 Initial and Boundary Conditions

The steady-state solution (velocity, pressure and temperature fields) for a stratified two-fluid flow with heat transfer in a clean channel (without deposit) is used as the initial condition. To obtain this steady-state solution, the following boundary conditions are enforced with the exception of those for C (which is not solved). Then only at $t = 0$, fluid 1 starts to carry particles of concentration C_o into the

channel initializing the deposition process. This mimics the real practical situation where deposition starts from a clean channel.

The following boundary conditions apply:

At the inlet ($x = 0$)

$$u = \begin{cases} u_1 & 0 \le y \le 0.5H \\ u_2 & 0.5 \le y \le H \end{cases},\ v = 0,\ C = \begin{cases} C_o & 0 \le y \le 0.5H \\ 0 & \text{otherwise} \end{cases},\ T = T_{in} \tag{24a}$$

At the outlet ($x = L$)

$$\frac{\partial u}{\partial x} = 0,\ v = 0,\ \frac{\partial C}{\partial x} = 0,\ \frac{\partial T}{\partial x} = 0 \tag{24b}$$

At the wall ($y = 0$ and $y = H$)

$$\vec{u} = \vec{0},\ \frac{\partial C}{\partial y} = 0,\ T = T_w \tag{24c}$$

3.5 Numerical Method

The conservation equations (Eqs. 8-11) can be recast into a general equation of the form,

$$\frac{\partial(\tilde{\rho}\Phi)}{\partial t} + \nabla \bullet (\tilde{\rho}\vec{u}\Phi) = \nabla \bullet (\tilde{\Gamma}\nabla\Phi) + S \tag{25}$$

where $\tilde{\rho}$, $\tilde{\Gamma}$, and S are the "appropriate" density, diffusion coefficient and source term, respectively. This general equation is solved using a Finite Volume Method. The velocity-pressure coupling is handled with the SIMPLER algorithm [32]. A 2nd order upwind scheme with superbee limiter [33] is used for the convective term and a fully implicit scheme is used for time integration.

The level-set (Eqs. 2 and 4) is spatially discretized with WENO5 [34]. This higher order scheme allows portions of the front with large curvature to be captured more accurately. TVD-RK2 (Total-Variational-Diminishing 2nd order Runge-Kutta scheme) [35] is employed to ensure numerical

stability in the temporal integration of the level-set function. To reduce the computational effort, the level-set method is implemented in a narrow-band procedure [36] where the level-set function is solved only within a band of certain thickness from the interface.

3.6 Solution Algorithm

The solution procedure can be summarized as follows:

(1) Specify the initial conditions (i.e. $t = 0$) of ϕ_f, ϕ_d, $\vec{u}$, p, C and T.

(2) Advance the time step to $t + \Delta t$.

(3) Solve Eqs. (2) for $\phi_f\big|^{t+\Delta t}$ and (4) for $\phi_d\big|^{t+\Delta t}$.

(4) Solve Eqs. (8) and (9) for $\vec{u}\big|^{t+\Delta t}$ and $p\big|^{t+\Delta t}$.

(5) Solve Eq. (10) for $C\big|^{t+\Delta t}$.

(6) Solve Eq. (11) for $T\big|^{t+\Delta t}$.

(7) Repeat steps (3) to (6) until the solution converges.

(8) Perform local mass correction for $\phi_f\big|^{t+\Delta t}$ [29].

(9) Perform particle redistribution [17].

(10) Repeat steps (2) to (9) for all time steps.

3.7 Verifications

Verification of the current numerical framework for particle deposition in single-fluid [17] and two-fluid [26] flow environments have been conducted. Besides, verifications for multi-fluid flow were also performed [37]. These will not be repeated here. Only verification of the heat transfer aspect of

the framework will be presented here. Since heat transfer in two-fluid flow with a growing deposit layer is not possible at the moment due to the unavailability of similar work, verification will then be based on known solutions of two limiting heat transfer cases for: (1) stratified single-fluid channel flow and (2) single-fluid channel flow with a growing deposit layer.

In the first verification exercise, heat transfer for a stratified two-fluid flow in a clean channel is considered. The length to height ratio of the channel is set to $L:H=3:1$. Two immiscible fluids flow into the channel with the same inlet velocity and temperature. No slip boundary condition is enforced at the upper and lower walls. These two walls are maintained at constant temperature. Fully-developed condition is assumed at the outlet. The physical properties of the two fluids are then purposely chosen to be identical. With identical properties, the problem reduces to heat transfer in a single-fluid channel flow, i.e. the Graetz problem. The exact Nusselt number at the fully-developed region can obtained analytically as 7.54 and is independent of Re. Given the symmetry of the problem, the local Nusselt number Nu_x at both the upper and the lower wall are identical. Therefore, only the Nu_x at the lower wall is calculated from the present numerical solutions as

$$Nu_x = \frac{2H}{T_w - T_b}\left.\frac{\partial T}{\partial y}\right|_{y=0} \tag{26a}$$

where the bulk temperature T_b is determined using

$$T_b = \int_0^H |u|\rho c_p T dy \Big/ \int_0^H |u|\rho c_p dy \tag{26b}$$

Plotted in Fig. 2 is Nu_x along the channel for two different Reynolds numbers of $\mathrm{Re}=5$ and $\mathrm{Re}=10$. Nu_x for both Re converge to the value of 7.55 at the fully-developed flow region. This is in very close agreement with the exact value of 7.54.

In the second verification exercise, again the properties of the two fluids are set to be identical. With this, the solution should reduce to that of heat transfer for a single-fluid channel flow with a growing

deposit layer internally. Figure 3 shows sequentially the deposit profile, the Nusselt number at the lower (Nu_{lx}) and the upper (Nu_{ux}) walls. Note that Nu_{lx} and Nu_{ux} are defined respectively as

$$Nu_{lx} = \frac{(H-\delta)}{T_d - T_b} \left. \frac{\partial T}{\partial \vec{n}_d} \right|_{y=\delta} \tag{27a}$$

$$Nu_{ux} = \frac{(H-\delta)}{T_w - T_b} \left. \frac{\partial T}{\partial y} \right|_{y=H} \tag{27b}$$

where T_d and T_b are respectively the temperature at the fluid-deposit front and the bulk temperature. The bulk temperature is given by

$$T_b = \int_{\delta}^{H} \rho c_p |u| T dy \Big/ \int_{\delta}^{H} \rho c_p |u| dy \tag{27c}$$

The effect of the growing deposit layer has been accounted for in the calculation of Nu_{lx} and Nu_{ux} via Eqs. (27). Basically, the characteristic length is set to $H-\delta$, i.e. the local height of the channel not covered by the deposit and available for fluid flow. These definitions of Nusselt number will be used in all subsequent sections. From Figs. 3, the deposit profile, Nu_{lx} and Nu_{ux} are exactly identical to the expected results of a heat transfer problem in a single-fluid channel flow with a growing deposit layer [1]. This further verifies the implemented numerical framework.

4. Results and Discussion

4.1 Base Case

With the framework verified, the solution of a base case is first established to illustrate some of the heat transfer physics involved in a stratified two-fluid channel flow with a growing deposit layer. The domain employed is similar to that shown in Fig. 1. The length and height of the channel are respectively 2 and 1. The physical properties are chosen to have the ratios of $\rho_1 : \rho_2 : \rho_d = 5:4:5$, $\mu_1 : \mu_2 : \mu_d = 2:1:\infty$, $c_{p1} : c_{p2} : c_{pd} = 2:1:2$ and $k_1 : k_2 : k_d = 2:1:4$. The thickness of the two fluid

layers at the inlet is identical, i.e. $h_1 : h_2 = 1:1$. The inlet velocity of the fluids is set to a ratio of $u_1 : u_2 = 2:1$. The dimensionless concentration at the inlet is $C_o^* = 0.1$. With these, the relevant dimensionless numbers become $\mathrm{Re} = 4.8$, $\mathrm{Pr} = 6.96$, $Pe = 9$ and $Da = 10$. Computations are carried out using three different meshes: 80×40 control volumes (CVs) with $\Delta t = 4 \times 10^{-3}$, 160×80 CVs with $\Delta t = 2 \times 10^{-3}$, and 320×160 CVs with $\Delta t = 1 \times 10^{-3}$. The differences in Nu_{lx} at the fully-developed flow between these consecutively refined meshes are 2.8% and 0.7%, respectively. Therefore, a mesh size of 160×80 CVs with $\Delta t = 2 \times 10^{-3}$ is sufficient and will be employed in all following cases.

Figure 4 shows the transient velocity and dimensionless temperature (θ) fields with the interface and front superimposed. As mentioned above, the simulation starts from the steady-state velocity and temperature fields for a two-fluid *clean* channel flow shown in Fig. 4(a). The fluid 1 layer is progressively thicker along the flow direction due to its higher viscosity compared with that of fluid 2. Then at $t = 0$, fluid 1 starts carrying suspended particles into the channel. These particles deposit onto the lower wall of the channel gradually, forming a deposit layer. The growing deposit layer, which is impermeable and has different properties, changes the flow and temperature fields in a fully coupled manner. Generally, the deposit layer is thicker near the inlet due to a higher particle concentration and becomes thinner downstream as shown in Fig. 5(a). With more particles deposited on the wall along the flow direction, the amount of suspended particles in fluid 1 decreases. Therefore, fewer particles are deposited on the wall downstream, leading to a thinner deposit layer. As the deposit layer grows, fluid 1 and fluid-fluid interface are pushed upward. The less viscous fluid 2 layer is then squeezed into a much thinner layer in comparison with the fluid 1 layer.

Within the deposit layer near the inlet, heat is conducted both in the transverse and upstream directions. This component of upstream heat conduction is driven by the lower fluid temperature at the inlet. Also noted at any given axial location, the transverse temperature gradient is the smallest in the deposit layer; follow by that of fluid 1 and fluid 2. This is expected as the deposit has the highest thermal conductivity. The presence of the deposit layer has two opposite effects on heat transfer

performance. The deposit layer introduces an additional thermal resistance for the heat to be transferred from the wall to the fluid, directly lowering heat transfer performance. Of course, this additional thermal resistance increases with thicker deposit layer. However, the deposit layer also simultaneously reduces flow area, resulting in a higher local fluid velocity that augments convective heat transfer. Therefore, the overall heat transfer performance depends on the relative strength of these effects.

The effects of the deposit layer on Nu_{lx} and Nu_{ux} are plotted in Fig. 5. Figure 5(b) shows the variation of Nu_{lx} along the channel compared against to that of a clean channel, i.e. at time $t^*=0$. For a clean channel, along the flow direction, convective heat transfer decreases gradually as the fluid bulk temperature increases, therefore, both Nu_{lx} and Nu_{ux} decrease along the flow direction. Temporally, at the early stage prior to $t^*=7.5$, Nu_{lx} does not change much near the inlet (around $x^*<0.5$ where the deposit thickness grows from zero to a maximum thickness). However, at $t^*=11.25$, Nu_{lx} in this region becomes even lower than that of a clean channel, suggestive of a more dominating effect of increased thermal resistance due to a locally thicker deposit layer. However, it is interesting to note that Nu_{lx} downstream is larger than that in a clean channel. This is attributed to increased local fluid velocity in the presence of the deposit layer. Fluctuations in Nu_{lx} are observed at $t^*=7.5$ and $t^*=11.25$. Such kind of fluctuation in the Nusselt number is also observed in [38]. It is attributed to the increase/decrease of the temperature at the fluid-deposit front along the flow direction as the deposit layer grows. For example, a rise in the temperature at the fluid-deposit front increases T_d-T_b in Eq. (27a), in turn, decreases Nu_{lx}. Unlike Nu_{lx}, Nu_{ux} is consistently lower compared to that of a clean channel for all time. Note that the thickness of fluid 2 layer does not change much during the deposition process. With a smaller characteristic length of $H-\delta$ as the deposit layer grows, Nu_{ux} along the channel decreases with time. For example, at $t^*=11.25$ under fully developed flow, the flow area decreases about 30%, blocked by the deposit layer. However, the convection heat

transfer coefficient increases only around 20% given the accelerated velocity in a smaller area. Therefore, the Nu_{ux} decreases around 10% in the deposit channel compared with that of clean channel.

4.2 Effect of Inlet Velocity Ratio

The effect of the inlet velocity ratio is studied in this section. Four different inlet velocity ratios are considered, i.e. $u_1 : u_2 = 1:1$, $u_1 : u_2 = 1.5:1$, $u_1 : u_2 = 2:1$ and $u_1 : u_2 = 2.5:1$. The other dimensionless parameters are identical to those of the base case. Figure 6 shows the evolutions of the interface and deposit front for these inlet velocity ratios. Computationally, different velocity ratios are achieved by increasing u_1 with u_2 held fixed.

With a higher fluid 1 inlet velocity and therefore flowrate, at a given time although more particles are carried into the channel, these particles are driven more rapidly downstream. This reduces the likelihood of these particles deposited near the inlet. Instead of near the inlet region, more particles now deposit downstream. This results in a thinner deposit layer near the inlet and a thicker deposit layer downstream. As the deposit layer grows, the higher fluid 1 flowrate squeezes the fluid 2 layer to be thinner (Fig. 6a). The fluid-fluid interface is pushed upward to maintain continuity of shear stress at the interface. This can also be observed at the early stage in Fig. 6b where the deposit thickness for the four inlet velocity ratios is not significantly different.

The effect of inlet velocity ratio on heat transfer at the lower wall is shown in Fig. 7. With a higher inlet velocity ratio, Nu_{lx} is higher near the inlet but lower downstream. This variation in Nu_{lx} is intimately linked to the deposit thickness. Near the inlet, the thinner deposit layer which hinders heat transfer from hot wall to the fluid (for the case of a higher inlet velocity ratio) leads to a smaller thermal resistance. Coupled with higher convective heat transfer due to a higher u_1, Nu_{lx} increases. However, a thicker deposit layer downstream (for higher inlet velocity ratio) introduces a much higher thermal resistance, even offsetting the effect of increased convective heat transfer due to a higher u_1. As a result, Nu_{lx} decreases. For heat transfer at the upper wall, Nu_{ux} increases consistently with

higher inlet velocity ratio. The increase in fluid 1 flowrate squeezes fluid 2 into a thinner layer of a higher average velocity, leading to enhanced convective heat transfer performance.

4.3 Effect of Da Number

Damköhler number, i.e. Da, is an important parameter governing the deposition process. The variation of Da is attained by changing the deposition reaction rate r_d in Eq. (5). In this article, four different increasingly larger Da are studied, i.e. $Da = 1$, $Da = 5$, $Da = 10$ (base case) and $Da = 15$. The other dimensionless parameters are identical to those of the base case. Figure 9 shows the temporal evolution of the interface and the deposit front for these cases. The fluid-fluid interface for the clean channel without deposit at t^* = 0 is plotted in Fig. 9a serving as reference. Generally, a larger Da implies a faster deposition, as the deposition reaction rate r_d is larger. Therefore at a given time, a thicker deposit is formed for larger Da. This is particularly obvious at $t^* = 7.5$ and 11.25. For lower Da, a lot of the particles in contact with the fluid-deposit front are not deposit given the smaller deposition reaction rate. These particles will eventually be carried downstream. It is interesting to note that the deposit thickness downstream for $Da = 10$ and $Da = 15$ is close to each other. For these cases, most of the particles are already deposited upstream and therefore the amount of particles downstream is similarly low, leading to a similar deposit layer profile.

The effect of Da on Nu_{lx} is plotted in Fig. 10. Note that the deposit attains a maximum thickness slightly downstream of $x^* = 0.5$ (Fig. 9d), demarcating region of different heat transfer characteristics. For higher Da, the thicker deposit layer near the entrance ($x^* < 0.5$) introduces larger thermal resistance. The larger thermal resistance overcomes the effect of increase convective heat transfer due to a higher average fluid velocity. As a result, Nu_{lx} becomes lower. Downstream of $x^* = 0.5$, interestingly the opposite occurs, i.e. Nu_{lx} is higher for higher Da. This is attributed to increase in convective heat transfer due to a higher average fluid velocity (smaller flow area). Figure 11 shows the

plot of Nu_{ux} for different Da. Nu_{ux} is less affected by Da in region very near the inlet ($x^*=0.2$). For $x^*>0.2$, Nu_{ux} decreases with higher Da.

4.4 Effect of Thermal Conductivity Ratio

In this section, the effect of thermal conductivity ratio $k_1:k_2:k_d$ on heat transfer performance is studied. The other dimensionless parameters are identical to that of section 4.2 except now that the deposit thermal conductivity is varied. Note that flow and deposition are decoupled from energy transport. Therefore, the velocity field and the thickness of the deposit layer is identical to that of the base case in Figs. 4 and 5a, respectively. Four scenarios with increasingly higher deposit thermal conductivity are considered, i.e. $k_1:k_2:k_d=2:1:1$, $k_1:k_2:k_d=2:1:2$, $k_1:k_2:k_d=2:1:4$ and $k_1:k_2:k_d=2:1:6$. Nu_{lx} for these cases are plotted sequentially in Fig. 12. The increase of the deposit thermal conductivity reduces the thermal resistance for conduction heat transfer in the deposit layer from the lower hot wall, leading to a higher temperature at the fluid-deposit front. It is favourable for heat transfer as more heat could be taken away by the fluid through convective heat transfer between fluid 1 and the fluid-deposit front. This can be seen from Fig. 12a at $t^*=0.2$. Nu_{lx} for higher deposit thermal conductivity is slightly higher. However, it is not the case as time progresses. With more heat absorbs by fluid 1 for the case of higher deposit thermal conductivity over time, the fluid temperature increases significantly. This results in a smaller temperature difference between fluid 1 and fluid-deposit front downstream. Therefore, the potential for fluid 1 to convect heat reduces, leading to a lower Nu_{lx} downstream of $x^*=0.5$ (Figs. 12b, 12c and 12d). Figure 13 shows the variation of Nu_{ux} for different thermal conductivity ratio. Nu_{ux} increases consistently with the increase of deposit thermal conductivity. The increase of the thermal conductivity of the deposit layer reduces the thermal resistance which is favorable for heat transfer.

5. Conclusions

A numerical model is developed for moving boundary conjugate heat transfer in stratified two-fluid flows with a growing deposit layer. The model is applicable to other general moving boundary conjugate heat transfer problem in a two-fluid flow environment with deposition occuring simultaneously. Upon verification of the procedure, a base case is first studied to establish an understandings of the physical aspects of conjugate heat transfer in stratified two-fluid flows with a growing deposit layer. Then, the effects of inlet velocity ratio, Damköhler number and thermal conducitivty ratio on fluid flow characteristics and heat transfer performance are investigated. Some conclusions can be drawn:-

(1) Generally, the growth of the deposit layer pushes the fluid-fluid interface upwards. The deposit layer introduces additional thermal resistance (retards heat transfer) and reduces flow area (enhances convective heat transfer). The overall heat transfer performance depends on the relative strength of these two effects.

(2) The increase of fluid 1 inlet velocity increases Nu_{ux} consistently. However, the increase of fluid 1 inlet velocity increases Nu_{lx} upstream but decreases Nu_{lx} downstream due to the different deposit layer at upstream and downstream.

(3) Nu_{ux} decreases with the increase of Da number. A high Da number leads to low Nu_{lx} upstream and a high Nu_{lx} downstream.

(4) The increase of thermal conductivity of deposit layer increases Nu_{ux} along the flow channel. However, the increase of thermal conductivity of deposit layer only increases Nu_{lx} upstream. Nu_{lx} downstream decreases with the increase of the thermal conductivity of the deposit layer.

References

[1] L. Cheng, G. Ribatski, J.R. Thome, Two-phase flow patterns and flow-pattern maps: fundamentals and applications, Applied Mechanics Reviews 61 (2008) 050802-01-050802-28.

[2] J. Gong, Y. Zhang, L. Liao, J. Duan, P. Wang, J. Zhou, Wax deposition in the oil/gas two-phase flow for a horizontal pipe, Energy Fuels 25 (2011) 1624–1632.

[3] A. Rittirong, E. Panacharoensawad, C. Sarica, An experimental study of paraffin deposition under two-phase gas-oil slug flow in horizontal pipes, Offshore Technology Conference, OTC-26047-MS, 04-07 May 2015, Houston, Texas, USA.

[4] Z. Huang, M. Senra, R. Kapoor, H.S. Fogler, Wax deposition modeling of oil/water stratified channel flow, AIChE Journal 57 (2011) 841-851.

[5] A. Matzain, M.S. Apte, H.-Q. Zhang, M. Volk, J.P. Brill, J.L. Creek, Investigation of paraffin deposition during multiphase flow in pipelines and wellbores-part 1: experiments, Journal of Energy Resources Technology 124 (2002) 180–186.

[6] Z. Nasria, B. Dabir, Network modeling of asphaltene deposition during two-phase flow in carbonate, Journal of Petroleum Science and Engineering 116 (2014) 124–135.

[7] M.B. Bagheri, R. Kharrat, C. Ghotby, Experimental investigation of the asphaltene deposition process during different production schemes, Oil & Gas Science and Technology – Rev. IFP Energies nouvelles 66 (2011) 507-519.

[8] I. Rao, C.A. Koh, E.D. Sloan, A.K. Sum, Gas hydrate deposition on a cold surface in water-saturated gas systems, Industrial & Engineering Chemistry Research 52 (2013) 6262-6269.

[9] G.A. Hegde, A.K. Sum, T.J. Danielson, Multiphase flow modeling for gas hydrates in flow assurance, Offshore Technology Conference, OTC-25729-MS, 04-07 May 2015, Houston, Texas, USA.

[10] C.B. Panchal, B. Ljubicic, Designing two-phase flow heat exchangers for mitigating fouling, Proceedings of 7th International Conference on Heat Exchanger Fouling and Cleaning, Tomar, Portugal, July 1 - 6, 2007.

[11] M. Haghshenasfard, G.H. Yeoh, M. Dahari, K. Hooman, On numerical study of calcium sulphate fouling under sub-cooled flow boiling conditions, Applied Thermal Engineering 81 (2015) 18-27.

[12] M.S. Abd-Elhady, M.R. Malayeri, Transition of convective heat transfer to subcooled flow boiling due to crystallization fouling, Applied Thermal Engineering 92 (2016) 122-129.

[13] S.O. Unverdi, G. Tryggvason, A front-tracking method for viscous, incompressible, multi-fluid flows, Journal of Computational Physics 100 (1992) 25-37.

[14] C.W. Hirt, B.D. Nichols, Volume of fluid /VOF/ method for the dynamics of free boundaries, Journal of Computational Physics 39 (1981) 201-225.

[15] S. Osher, J.A. Sethian, Fronts propagating with curvature-dependent speed: algorithms based on Hamilton-Jacobi formulations, Journal of Computational Physics 79 (1988) 12-49.

[16] R. Banki, H. Hoteit, A. Firoozabadi, Mathematical formulation and numerical modeling of wax deposition in pipelines from enthalpy–porosity approach and irreversible thermodynamics, International Journal of Heat and Mass Transfer 51 (2008) 3387-3398.

[17] Q. Ge., Y.F. Yap, F.M. Vargas, M. Zhang, J.C. Chai, A total concentration method for modeling of deposition, Numerical Heat Transfer, Part B 61 (2012) 311-328.

[18] S.K. Beal, Correlations for the sticking probability and erosion of particles, Journal of Aerosol Science 9 (1978) 455-461.

[19] M.M. IslamRaja, M.A. Cappelli1, J.P. McVittie, K.C. Saraswat, A 3-dimensional model for low-pressure chemical-vapor-deposition step coverage in trenches and circular vias, Journal of Applied Physics 70 (1991) 7137-7140.

[20] F.M. Vargas, J.L. Creek, W.G. Chapman, On the development of an asphaltene deposition simulator, Energy & Fuel 24 (2010) 2294-2299.

[21] C. Heitzinger, S. Selberherr, On the Topography Simulation of Memory Cell Trenches for Semiconductor Manufacturing Deposition Processes Using the Level Set Method, Proceedings of 16th European Simulation Multiconference: Modelling and Simulation 2002 (ESM 2002), Jun. 3-5, Darmstadt, Germany, 653-660.

[22] Z. Adamczyk, M. Nattich-Rak, M. Sadowsk, A. Michna, K. Szczepaniak, Mechanisms of nanoparticle and bioparticle deposition – Kinetic aspects, Colloids and Surfaces A: Physicochemical and Engineering Aspects 439 (2013) 3–22.

[23] E. Ramirez-Jaramillo, C. Lira-Galeana, O. Manero, Modeling asphaltene deposition in production pipelines, Energy & Fuels 20 (2006) 1184-1196.

[24] M.S. Apte, A. Matzain, H.-Q. Zhang, M. Volk, J.P. Brill, J.L. Creek, Investigation of paraffin deposition during multiphase flow in pipelines and wellbores-part 2: Modeling, Journal of Energy Resources Technology 123 (2001) 150–186.

[25] Y.F. Yap, F.M. Vargas, J.C. Chai, A level-set method for convective-diffusive particle deposition, Applied Mathematical Modelling 37 (2013) 5245-5259.

[26] Y.F. Yap, A. Goharzadeh, F.M. Vargas, L.S. Biswal, J.C. Chai, Modeling of Particle Deposition in a Two-Fluid Flow Environment, International Journal of Heat and Fluid Flow (2016, submitted).

[27] H.Y. Li, Y.F. Yap, J. Lou, J.C. Chai, Z. Shang, Numerical investigation of conjugated heat transfer in a channel with a moving depositing front, International Journal of Thermal Sciences 88 (2015) 136-147.

[28] M. Sussman, P. Smereka, S. Osher, A level set approach for computing solutions to incompressible two-phase flow, Journal of Computational Physics 114 (1994) 146-159.

[29] Y.F. Yap, J.C. Chai, K.C. Toh, T.N. Wong, Y.C. Lam, Numerical modelling of unidirectional stratified flow with and without phase change, International Journal of Heat and Mass Transfer 48 (2005) 477-486.

[30] S. Chen, B. Merriman, S. Osher, P. Smereka, A simple level set method for solving Stefan problems, Journal of Computational Physics 135 (1995) 8-29.

[31] H.Y. Li, Y.F. Yap, J. Lou, Z. Shang, Numerical investigation of heat transfer in three-fluid stratified flows, International Journal of Heat and Mass Transfer 89 (2015) 576-587.

[32] S.V. Patankar, Numerical Heat Transfer and Fluid Flow. Hemisphere Publisher, New York, 1980.

[33] H.K. Versteeg, W. Malalasekera, An Introduction to Computational Fluid Dynamics: The Finite Volume Method, 2nd ed., Prentice Education Limited, England, 2007.

[34] G.S. Jiang, D. Peng, Weighted ENO schemes for Hamilton–Jacobi equations, SIAM Journal on Scientific Computing 21 (2000) 2126-2143.

[35] C.W. Shu, S. Osher, Efficient implementation of essentially non-oscillatory shock capturing schemes, Journal of Computational Physics 77 (1988) 439-471.

[36] D. Peng, B. Merriman, S. Osher, H. Zhao, M. Kang, A PDE-based fast local level-set method, Journal of Computational Physics 155 (1999) 410-438.

[37] H.Y. Li, Y.F. Yap, J. Lou, Z. Shang, Numerical modelling of three-fluid flow using the level-set method, Chemical Engineering Science 126 (2015) 224-236.

[38] S.H.-K. Lee, Y. Jaluria, Effects of streamwise convergence in radius on the laminar forced convection in axisymmetric ducts, Numerical Heat Transfer Part A 28 (1995) 19-38.

Figure Caption

Fig. 1 Domain of interest with two flowing fluids and a growing deposit layer.

Fig. 2 Verification against one-fluid flow.

Fig. 3 Verification against one-fluid flow with deposition (a) thickness of the deposit layer δ^*, (b) Nu_{lx}, and (c) Nu_{ux} at different times.

Fig. 4 Transient velocity and temperature fields for base case at (a) $t^*=0$, (b) $t^*=3.75$, (c) $t^*=7.5$, and (d) $t^*=11.25$.

Fig. 5 Variation of (a) the thickness of the deposit layer δ^*, (b) Nu_{lx}, and (c) Nu_{ux} at different times for base case.

Fig. 6 The fluid-fluid interface and the fluid-deposit front for cases with different inlet velocity ratios at (a) $t^*=0$, (b) $t^*=3.75$, (c) $t^*=7.5$, and (d) $t^*=11.25$.

Fig. 7 Variation of Nu_{lx} for cases with different inlet velocity ratios at (a) $t^*=3.75$, (b) $t^*=7.5$, and (c) $t^*=11.25$.

Fig. 8 Variation of Nu_{ux} for cases with different inlet velocity ratios at (a) $t^*=3.75$, (b) $t^*=7.5$, and (c) $t^*=11.25$.

Fig. 9 The fluid-fluid interface and the fluid-deposit front for cases with different Da at (a) $t^*=0$, (b) $t^*=3.75$, (c) $t^*=7.5$, and (d) $t^*=11.25$.

Fig. 10 Variation of Nu_{lx} for cases with different Da at (a) $t^*=3.75$, (b) $t^*=7.5$, and (c) $t^*=11.25$.

Fig. 11 Variation of Nu_{ux} for cases with different Da at (a) $t^*=3.75$, (b) $t^*=7.5$, and (c) $t^*=11.25$.

Fig. 12 Variation of Nu_{lx} for cases with different thermal conductivity ratio at (a) $t^*=0.375$, (b) $t^*=3.75$, (c) $t^*=7.5$, and (d) $t^*=11.25$.

Fig. 13 Variation of Nu_{ux} for cases with different thermal conductivity ratio at (a) $t^*=0.375$, (b) $t^*=3.75$, (c) $t^*=7.5$, and (d) $t^*=11.25$.

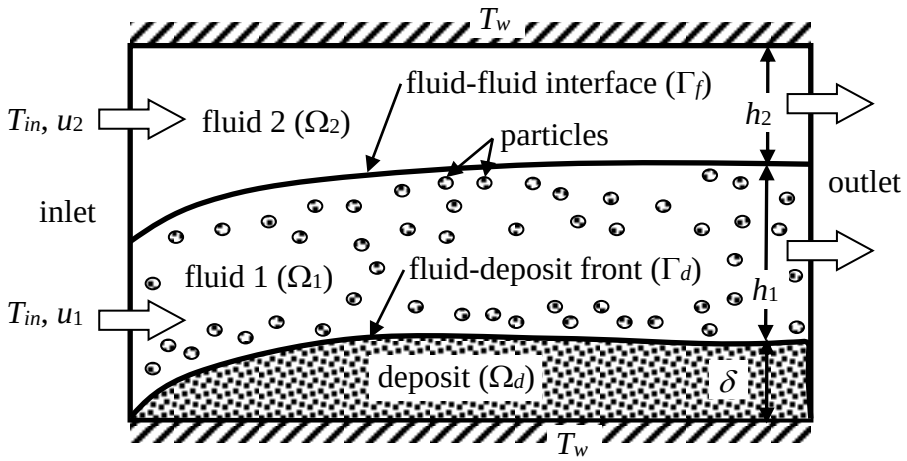

Fig. 1 Domain of interest with two flowing fluids and a growing deposit layer.

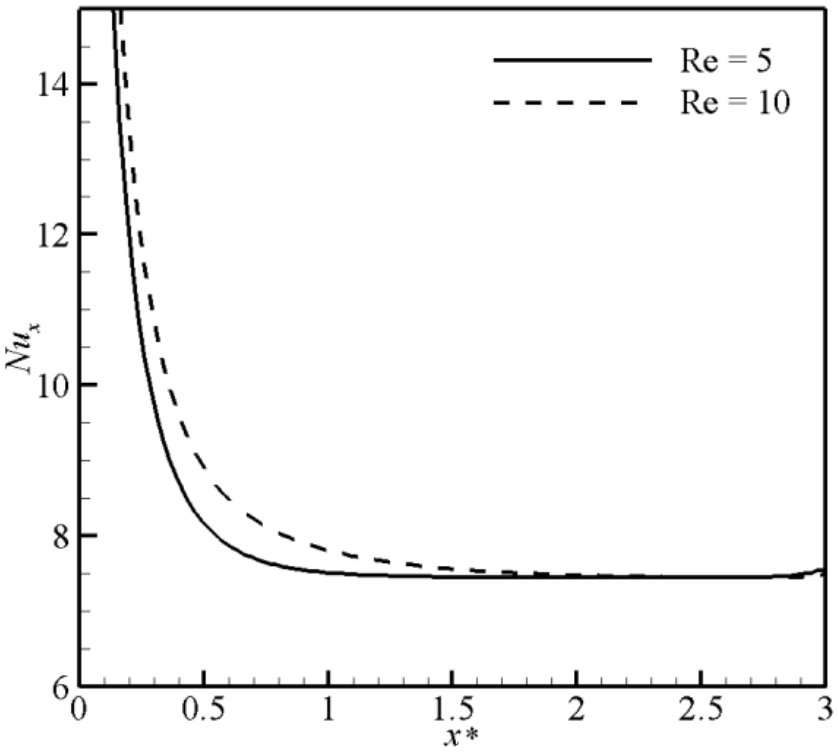

Fig. 2 Verification against one-fluid flow.

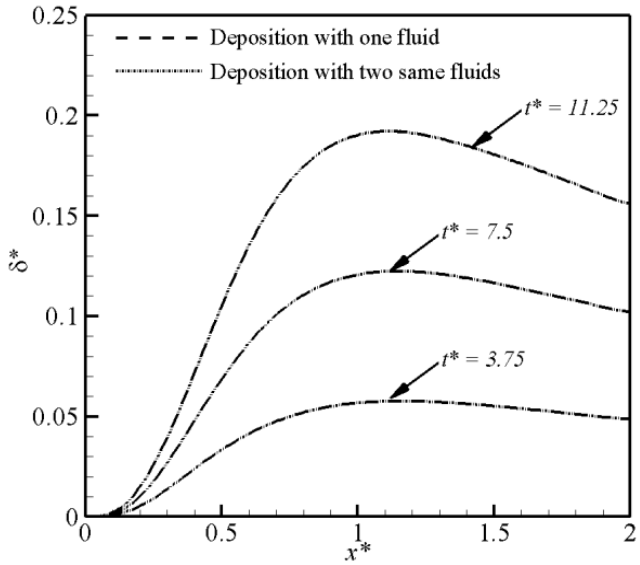

(a)

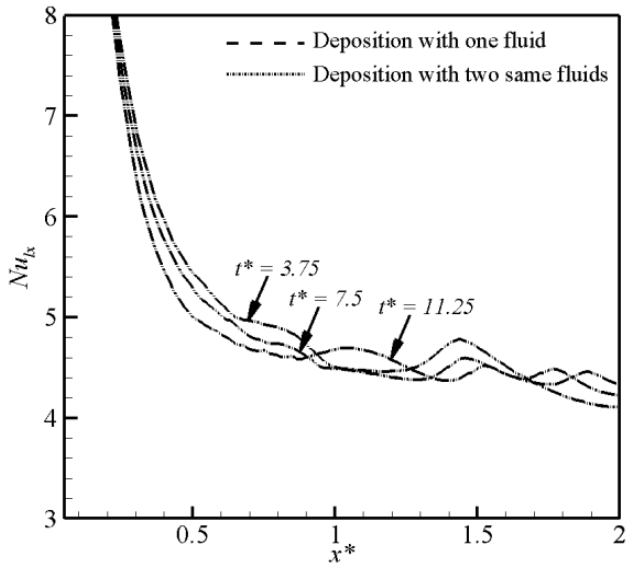

(b)

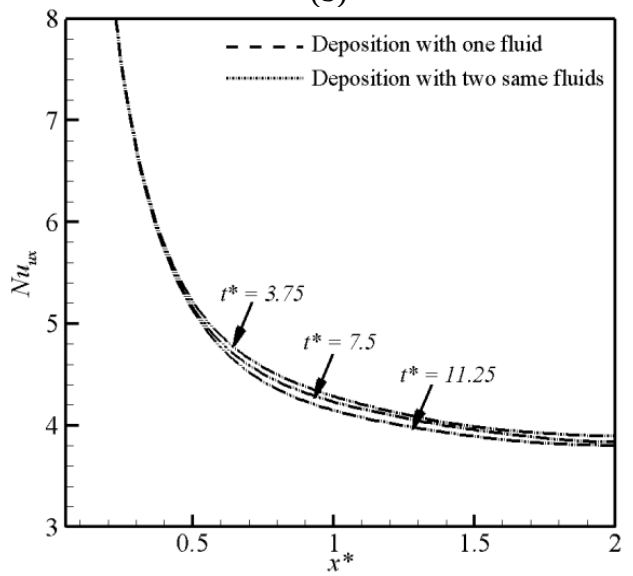

(c)

Fig. 3 Verification against one-fluid flow with deposition (a) thickness of the deposit layer $\delta*$, (b) Nu_{lx}, and (c) Nu_{ux} at different times.

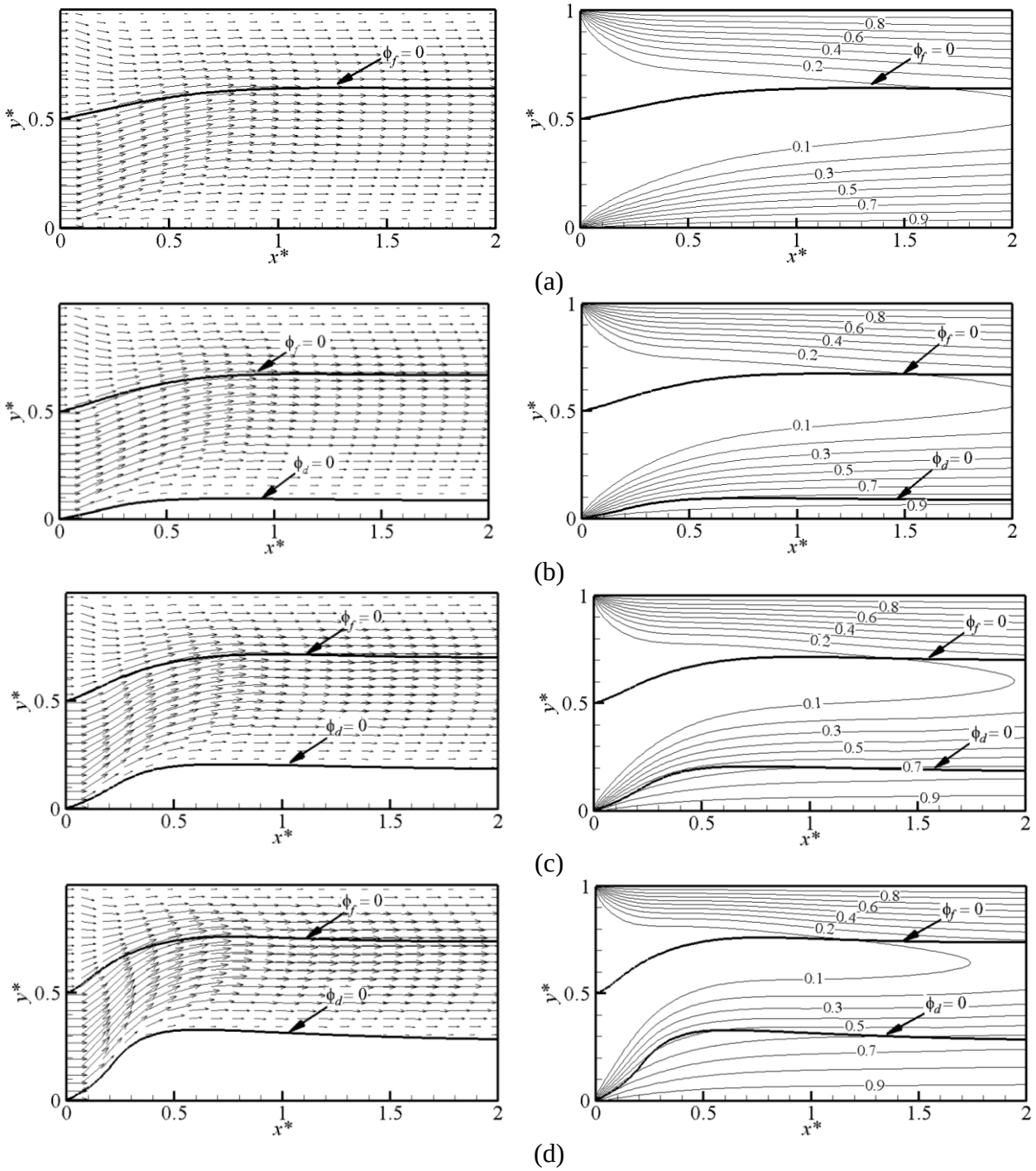

Fig. 4 Transient velocity and temperature fields for base case at (a) $t^* = 0$, (b) $t^* = 3.75$, (c) $t^* = 7.5$, and (d) $t^* = 11.25$.

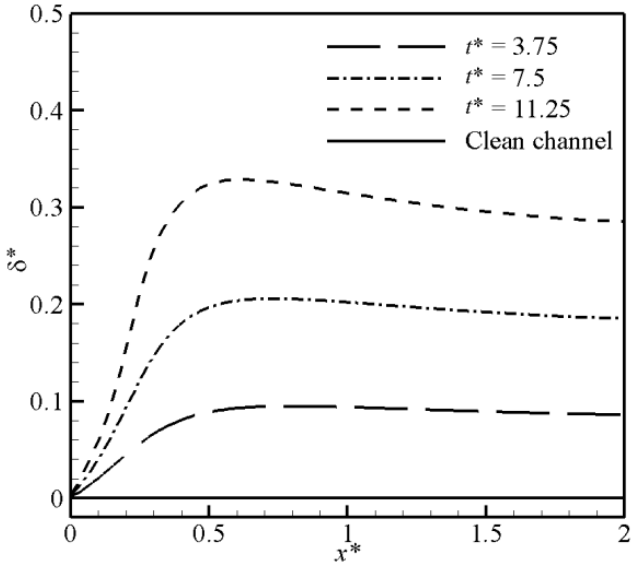

(a)

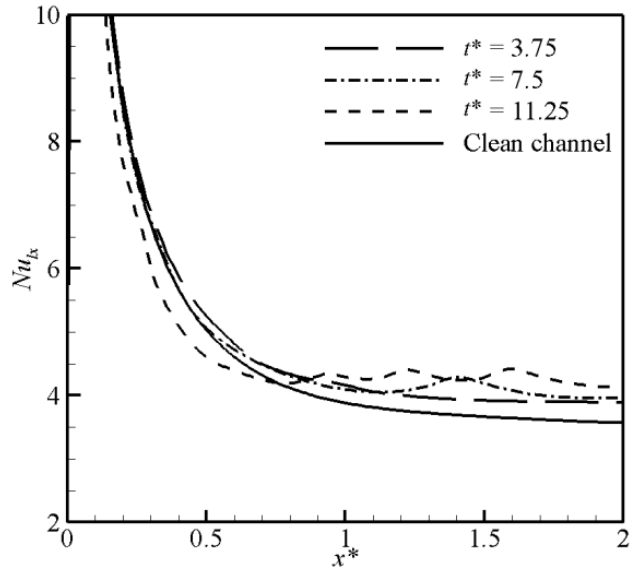

(b)

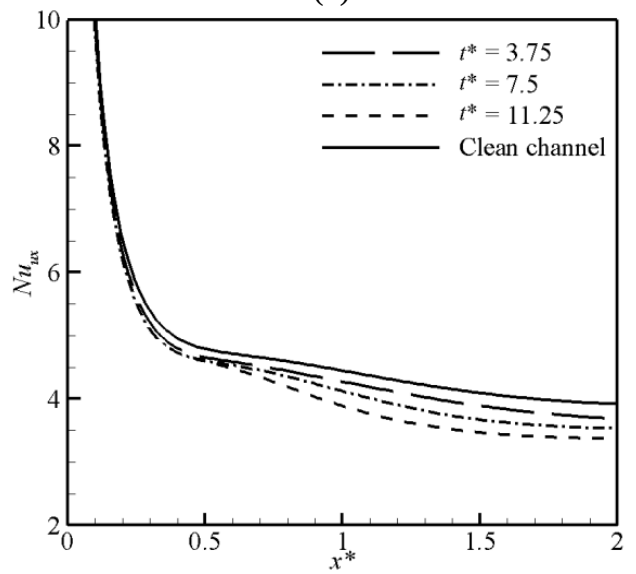

(c)

Fig. 5 Variation of (a) the thickness of the deposit layer $\delta*$, (b) Nu_{lx}, and (c) Nu_{ux} at different times for base case.

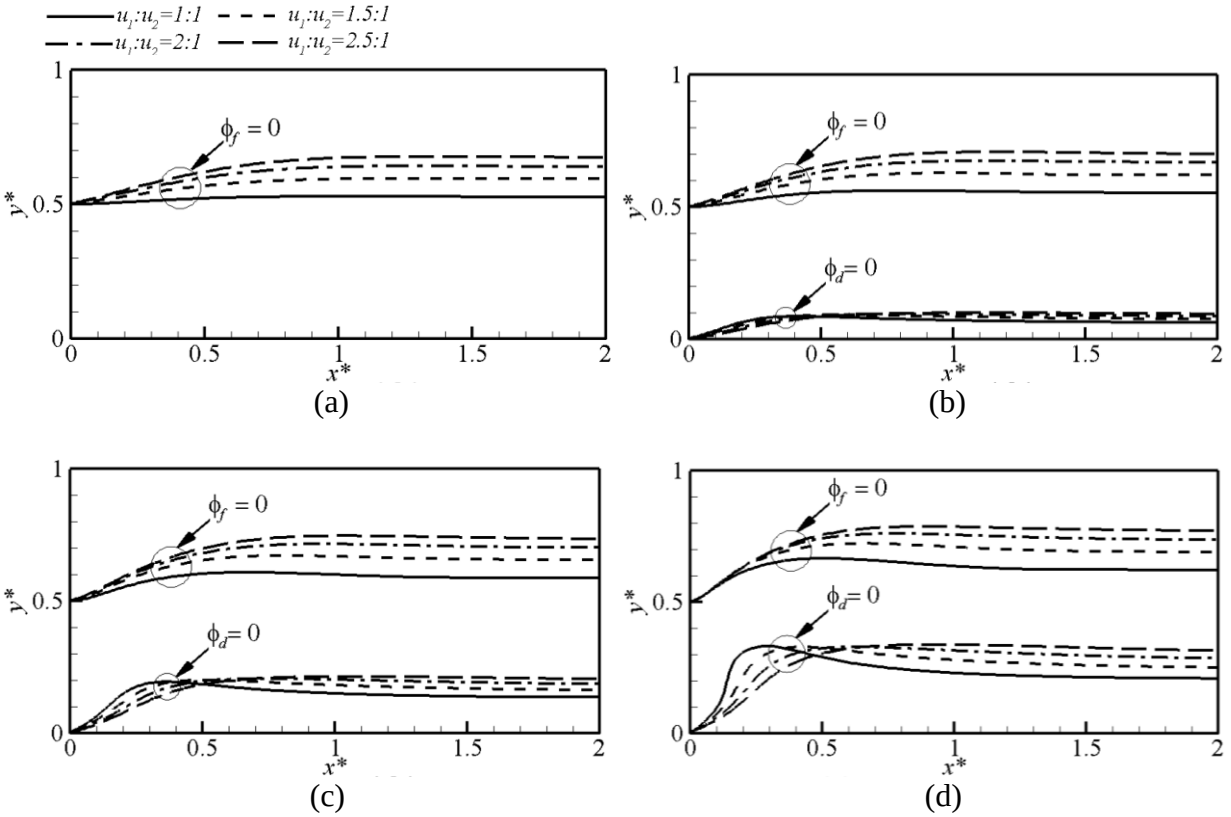

Fig. 6 The fluid-fluid interface and the fluid-deposit front for cases with different inlet velocity ratios at (a) $t^*=0$, (b) $t^*=3.75$, (c) $t^*=7.5$, and (d) $t^*=11.25$.

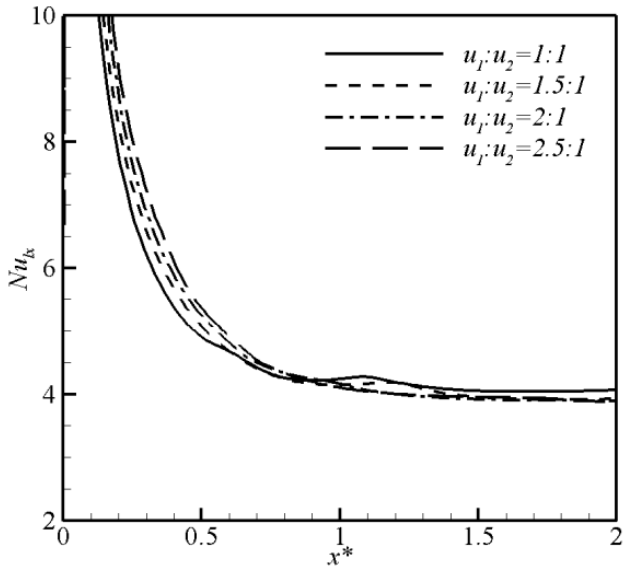

(a)

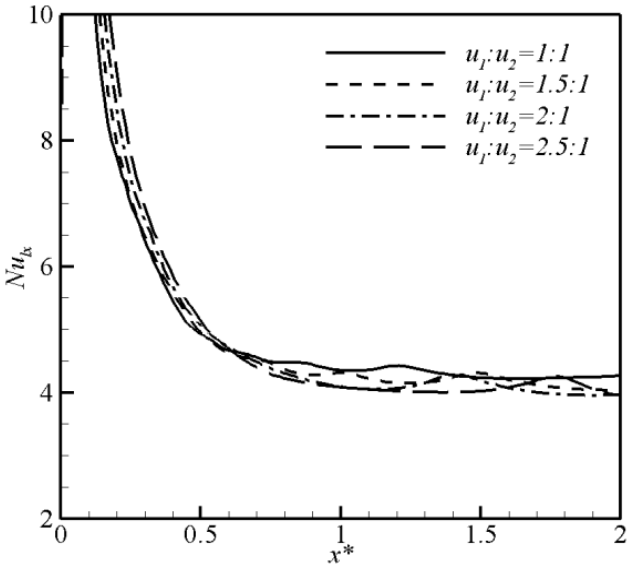

(b)

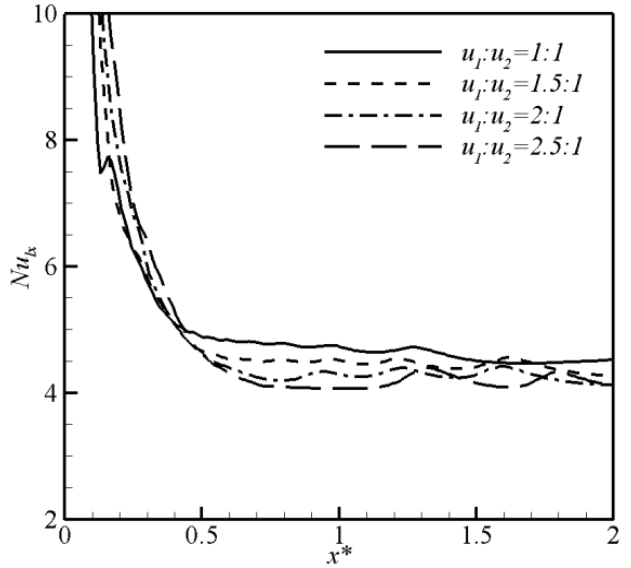

(c)

Fig. 7 Variation of Nu_{l_x} for cases with different inlet velocity ratios at (a) $t^*=3.75$, (b) $t^*=7.5$, and (c) $t^*=11.25$.

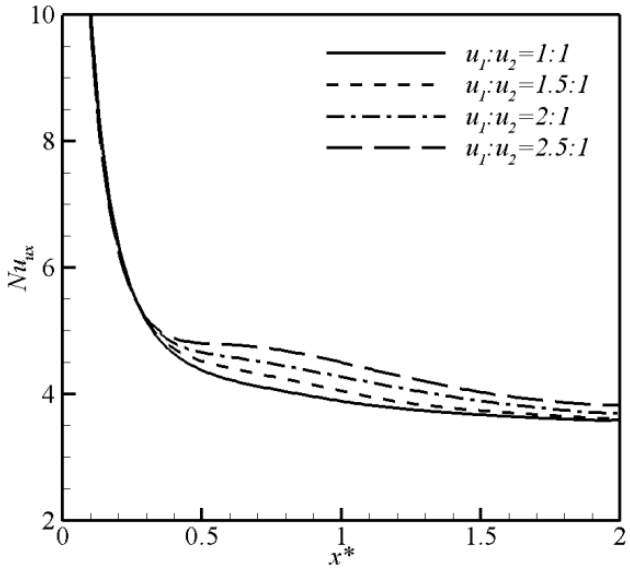

(a)

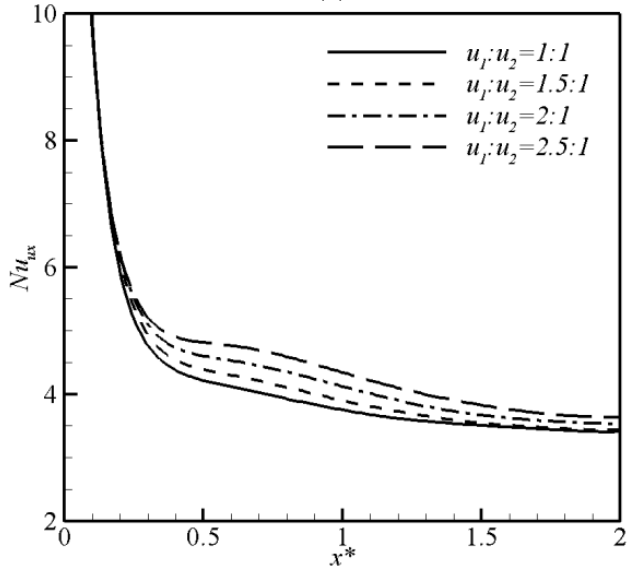

(b)

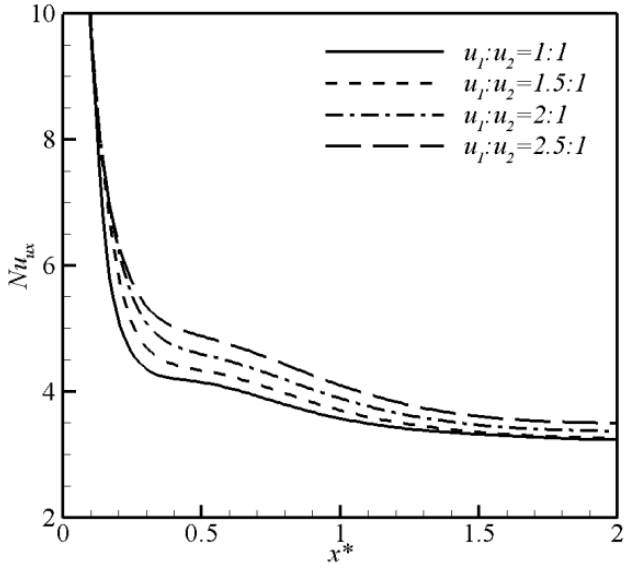

(c)

Fig. 8 Variation of Nu_{ux} for cases with different inlet velocity ratios at (a) $t^*=3.75$, (b) $t^*=7.5$, and (c) $t^*=11.25$.

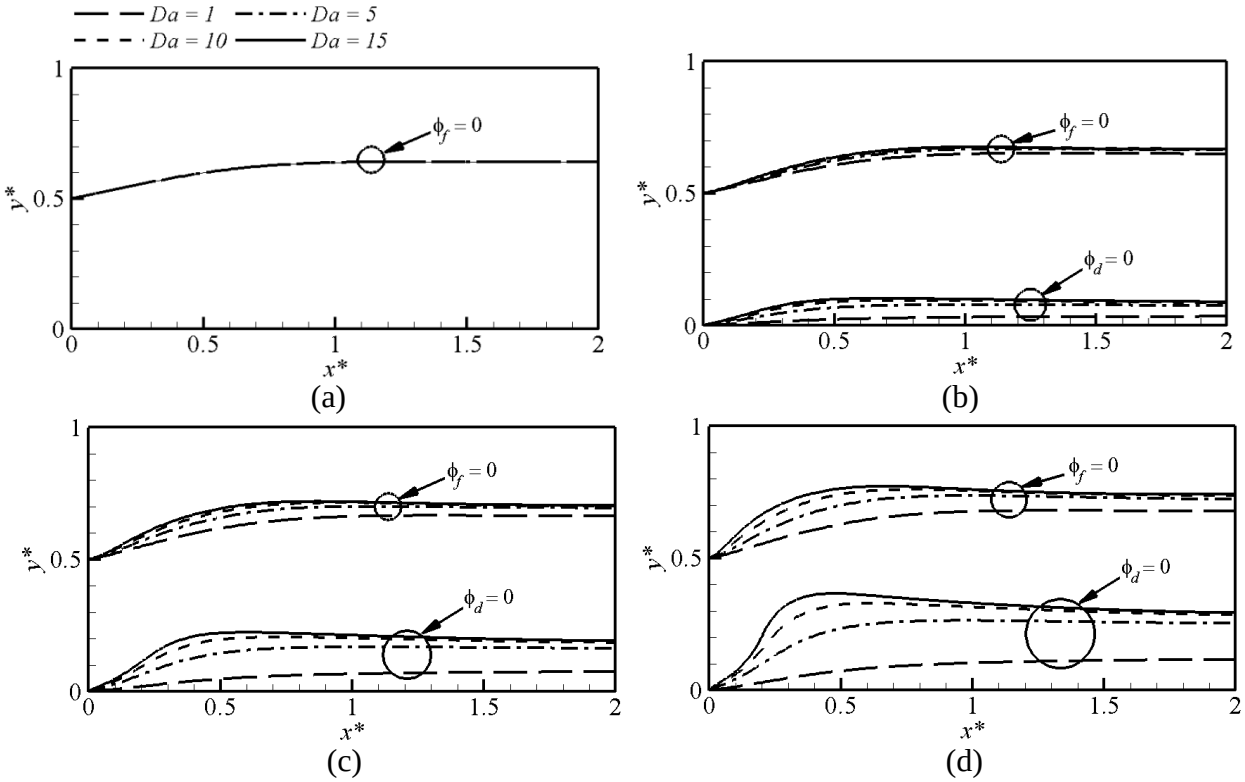

Fig. 9 The fluid-fluid interface and the fluid-deposit front for cases with different Da at (a) $t^* = 0$, (b) $t^* = 3.75$, (c) $t^* = 7.5$, and (d) $t^* = 11.25$.

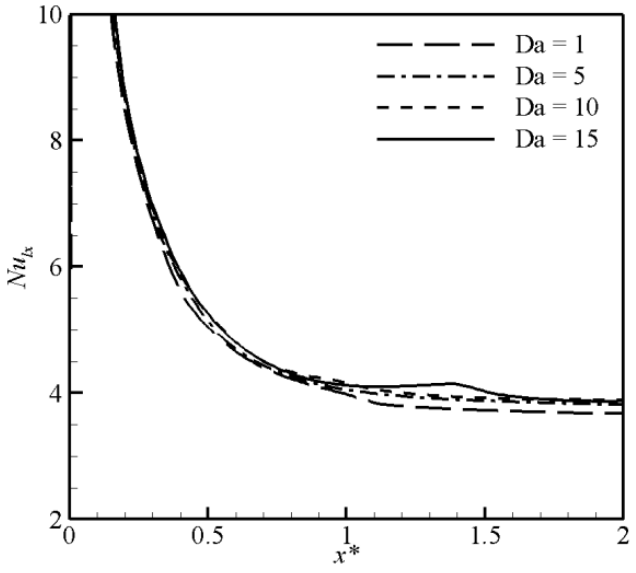

(a)

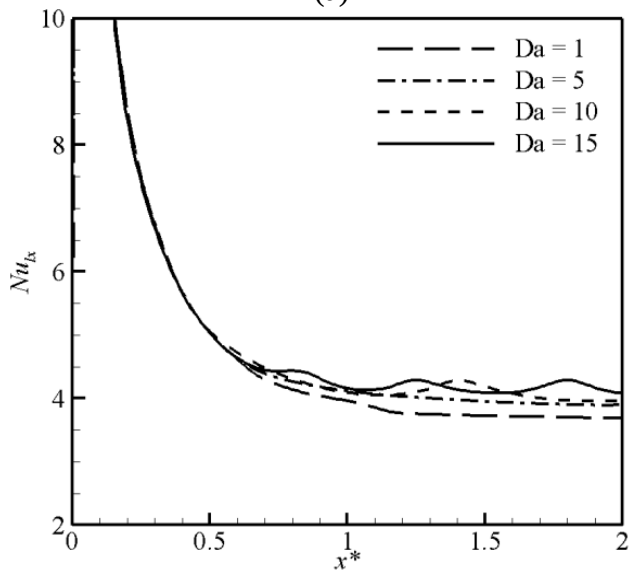

(b)

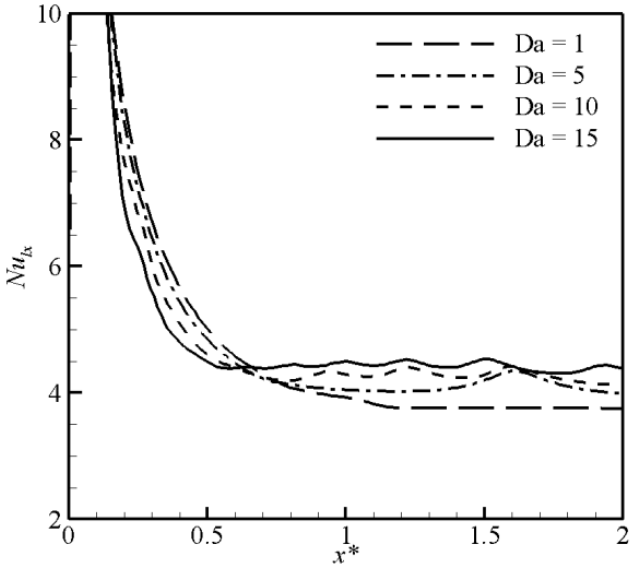

(c)

Fig. 10 Variation of Nu_{lx} for cases with different Da at (a) $t^*=3.75$, (b) $t^*=7.5$, and (c) $t^*=11.25$.

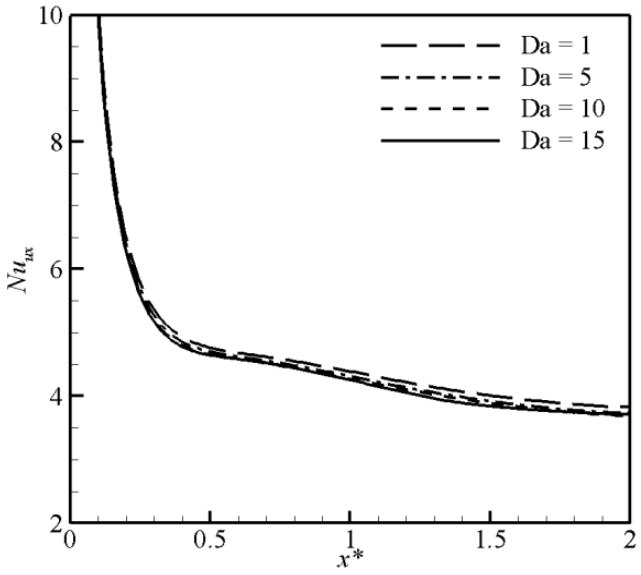

(a)

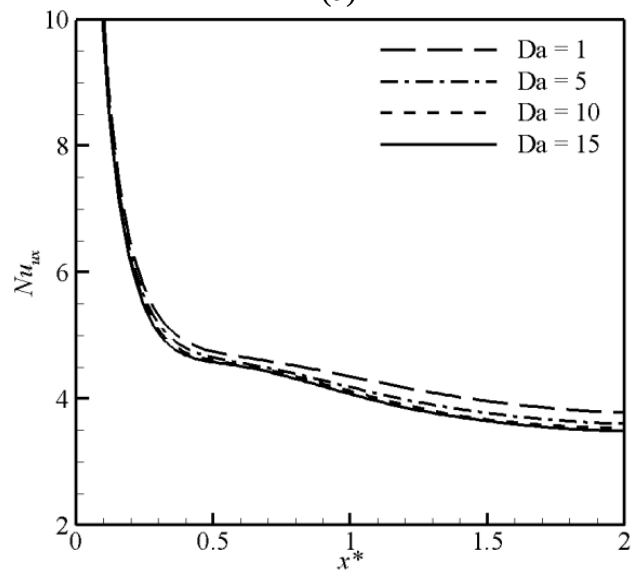

(b)

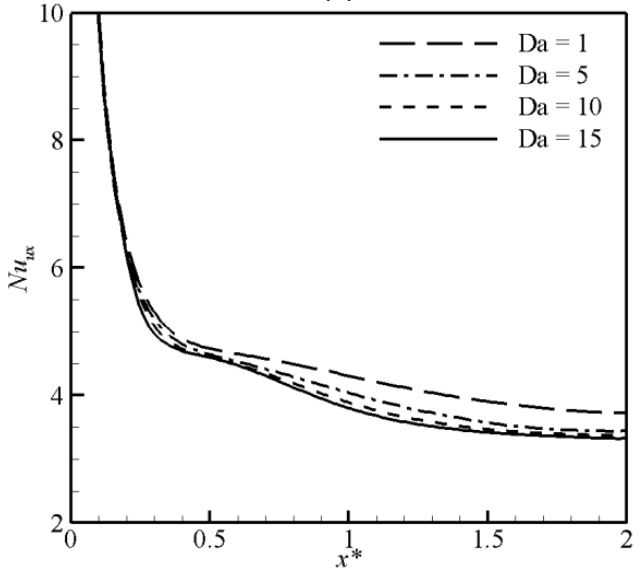

(c)

Fig. 11 Variation of Nu_{ux} for cases with different Da at (a) $t^*=3.75$, (b) $t^*=7.5$, and (c) $t^*=11.25$.

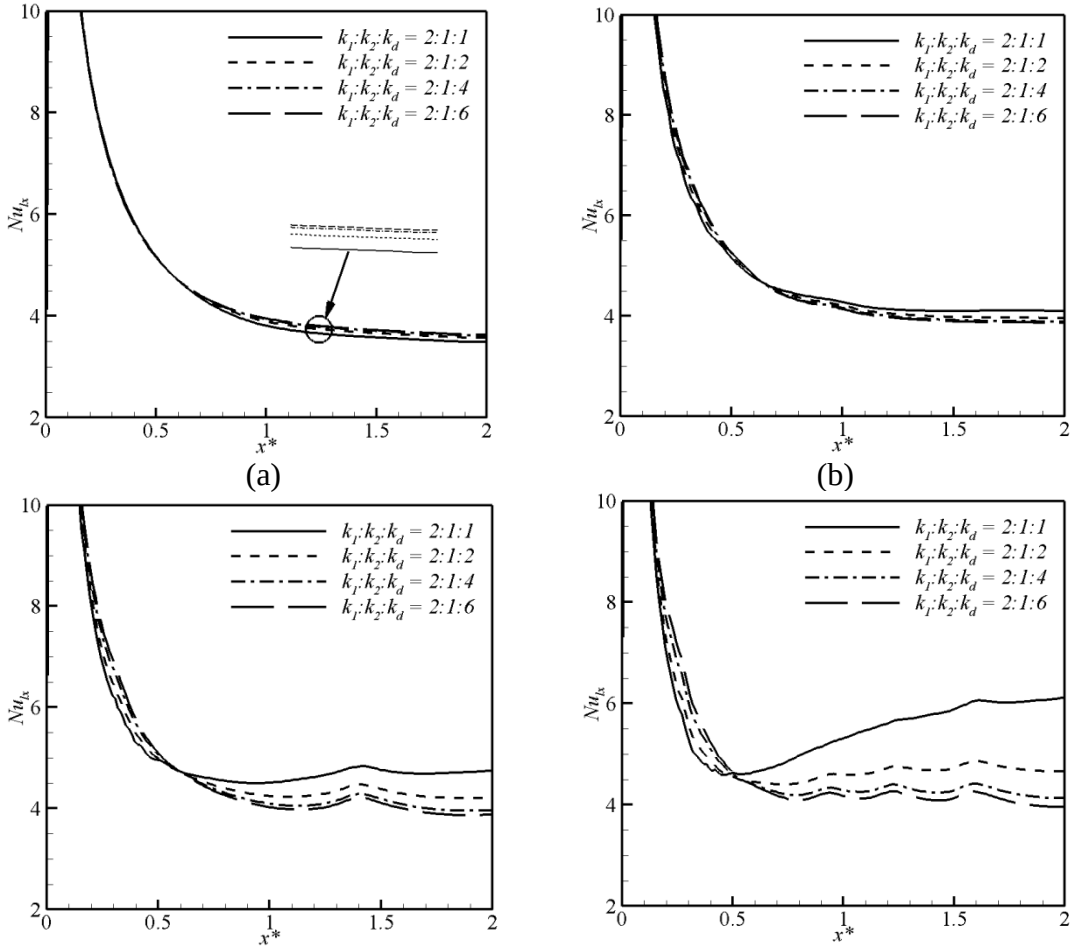

Fig. 12 Variation of Nu_{lx} for cases with different thermal conductivity ratio at (a) $t^*=0.375$, (b) $t^*=3.75$, (c) $t^*=7.5$, and (d) $t^*=11.25$.

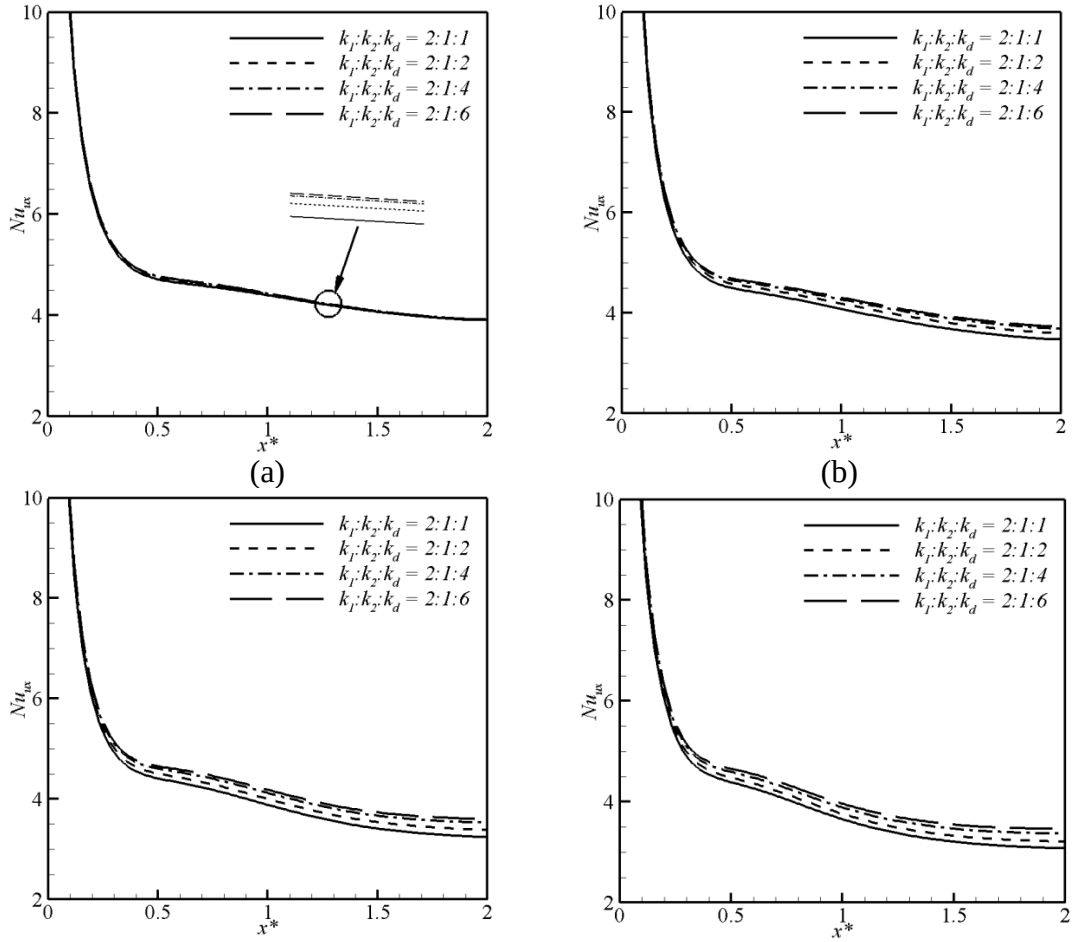

Fig. 13 Variation of Nu_{ux} for cases with different thermal conductivity ratio at (a) $t^*=0.375$, (b) $t^*=3.75$, (c) $t^*=7.5$, and (d) $t^*=11.25$.